Reduced Enthalpy of Metal Hydride Formation for Mg–Ti Nanocomposites Produced by Spark Discharge Generation

Anca Anastasopol,[†] Tobias V. Pfeiffer,[‡,§] Joost Middelkoop,[§] Ugo Lafont,[∥] Roger J. Canales-Perez,[‡] Andreas Schmidt-Ott,[‡,§] Fokko M. Mulder,[†,§] and Stephan W.H. Eijt*[,†]

[†]Fundamental Aspects of Materials and Energy, Department of Radiation, Radionuclides and Reactors, Faculty of Applied Sciences, Delft University of Technology, Delft, The Netherlands

[‡]NanoStructured Materials, Department of Chemical Engineering, Faculty of Applied Sciences, Delft University of Technology, Delft, The Netherlands

[§]Materials for Energy Conversion and Storage, Department of Chemical Engineering, Faculty of Applied Sciences, Delft University of Technology, Delft, The Netherlands

[∥]Novel Aerospace Materials, Department of Aerospace Structures and Materials, Faculty of Aerospace Engineering, Delft University of Technology, Delft, The Netherlands

ABSTRACT: Spark discharge generation was used to synthesize Mg–Ti nanocomposites consisting primarily of a metastable body-centered-cubic (bcc) alloy of Mg and Ti. The bcc Mg–Ti alloy transformed upon hydrogenation into the face-centered-cubic fluorite $Mg_{1-y}Ti_yH_x$ phase with favorable hydrogen storage properties. Both metal and metal hydride nanocomposites showed a fractal-like porous morphology, with a primary particle size of 10–20 nm. The metal content of 70 atom % (at %) Mg and 30 at % Ti, consistently determined by XRD, TEM-EDS, and ICP-OES, was distributed uniformly across the as-prepared sample. Pressure–composition isotherms for the Mg–Ti–H nanocomposites revealed large differences in the thermodynamics relative to bulk MgH_2, with a much less negative enthalpy of formation of the hydride as small as -45 ± 3 kJ/molH$_2$ as deduced from van't Hoff plots. The plateau pressures of hydrogenation were substantially higher than those for bulk MgH_2 in the low temperature range from 150 to 250 °C. The reaction entropy was simultaneously reduced to values down to 84 ± 5 J/K mol H$_2$, following a linear relationship between the enthalpy and entropy. Plausible mechanisms for the modified thermodynamics are discussed, including the effect of lattice strains, the presence of interfaces and hydrogen vacancies, and the formation of excess free volume due to local deformations. These mechanisms all rely on the finely interdispersed nanocomposite character of the samples which is maintained by grain refinement.
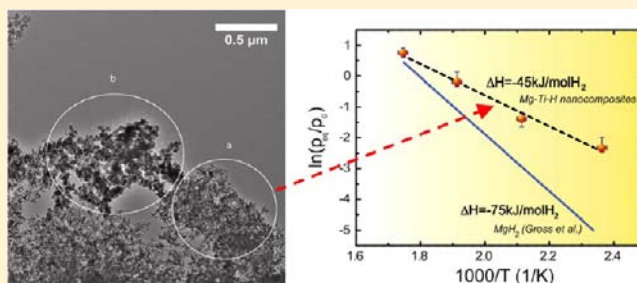
INTRODUCTION

The use of hydrogen as an energy carrier for mobile applications brings the requirement of a compact but also light storage material.[1,2] It is well-known that several metals can absorb large amounts of hydrogen, forming more compact storage media than hydrogen gas tanks and liquid hydrogen.[1] However, most metals have a relatively poor gravimetric capacity.[2] Among several metals, Mg represents an attractive candidate as a hydrogen storage material for its light weight and reversible character of the hydrogen sorption reactions. The relatively slow kinetics of the reaction of Mg with hydrogen is in a first instance addressed by decreasing the size of the Mg particles to limit diffusion distances. Other routes of enhancing the sorption kinetics consist of inducing defects in the crystal structure to enhance hydrogen mobility and mixing Mg with transition metals acting as catalysts.[3]

Spark discharge generation is a versatile method of producing metal nanoparticles. Nanostructured materials for hydrogen storage are commonly produced by ball milling. One of the main advantages of spark discharge generation as opposed to ball milling is the synthesis of nanoparticles instead of just nanocrystalline grains, in a continuous rather than batch-wise process. In previous studies,[4,5] transition metal (Pd, Nb) catalyzed Mg nanoparticles have been successfully synthesized by spark discharge generation. Through this bottom up method of producing nanoparticles, small scale mixing of the Mg with transition metal catalysts is successfully achieved. Because of the nonequilibrium nature of the particle production, metastable alloys can also be produced by spark discharge generation.[6] Other bottom-up approaches involving inert gas condensation methods[7−9] focused thus far on the synthesis of elemental Mg nanoparticles. Further, Mg-based and MgH_2-based nano-particles for hydrogen storage applications were produced by
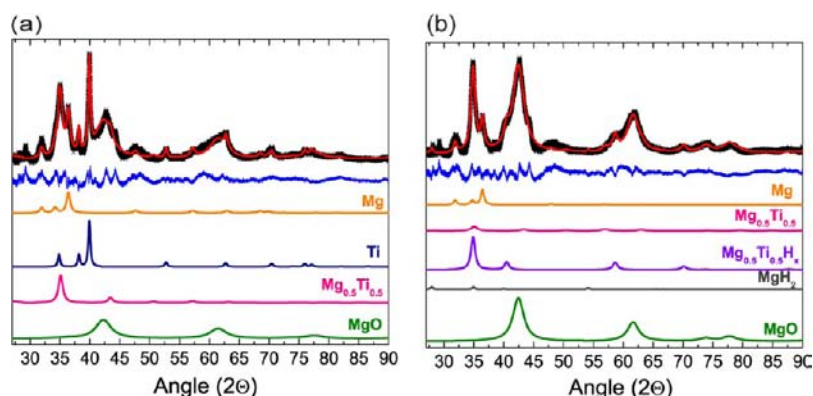
Figure 1. X-ray diffraction patterns of the spark discharge generated Mg−Ti nanocomposites, and the results of the Rietveld refinement (measured spectra, black; calculated spectra, red; residual, blue): (a) as produced by spark discharge generator; (b) after partial loading with hydrogen. The background due to the sample container was subtracted. The individual phase contributions are given below (scaled down by a factor of 0.5).

melt infiltration[10,11] and by decomposition of organometallic precursors under suitable conditions.[12,13] To the best of our knowledge, the synthesis of Mg−Ti alloy nanoparticles by bottom-up methods has not been reported before.

The ability of Mg to react with hydrogen is in a great measure influenced by its enthalpy of formation which is experimentally determined to be about −75 kJ/mol H_2. A lower enthalpy of formation for Mg combined with improved kinetics would allow the reaction with hydrogen to proceed at much milder conditions of temperature and pressure than currently employed. Recent studies revealed that the interaction between Mg and Ti offers several opportunities to modify the thermodynamics and kinetics of the hydrogenation reaction. Intense research has shown that the use of nonequilibrium synthesis techniques, such as magnetron sputter deposition[14−18] of Mg−Ti thin films, may result in the formation of an hcp Mg−Ti coherent phase despite the positive enthalpy of mixing of Mg and Ti. Upon hydrogenation of the Mg−Ti thin films, a cubic fluorite $Mg_{1-y}Ti_yH_x$ phase was formed for Ti-fractions above ~15 atom % (at %), with favorable hydrogen sorption kinetics. The hydrogen absorption equilibrium pressure of multilayer thin films consisting of alternating Mg and Ti nanolayers[19] is significantly higher than the equilibrium pressures of bulk MgH_2 and TiH_2. The use of thin films as hydrogen storage devices, however, has obvious strong limitations. For this reason, intense research is being carried out on the synthesis of Mg−Ti−H alloys by means of ball-milling.[20−22] The first Mg−Ti hydride phase, a cubic Mg_7TiH_{16} compound, was found by Kyoi et al.[23] using a high pressure synthesis method.

In the present study, Mg−Ti nanocomposites are synthesized using spark discharge generation. Alongside the presence of Mg and Ti nanoparticles, a nanosized, metastable intermetallic body-centered-cubic Mg−Ti alloy phase has been identified in the as-prepared samples. The very low solubility of Mg in Ti (and of Ti in Mg) makes the presence of this cubic Mg−Ti phase an interesting result in itself. Moreover, a detailed structure analysis of the hydrogenation products showed the formation of the cubic fluorite Mg−TiH_x hydride phase, which remains in a nanoparticle state after long hydrogenation heating treatments. Our pressure−composition−temperature (PCT) measurements obtained using a Sievert's apparatus revealed a much less negative enthalpy of formation of −45 ± 3 kJ/mol H_2. Such a small value for the enthalpy of formation for the Mg−Ti−H system has not been reported before. Essentially,

the plateau pressures are significantly higher than for bulk MgH_2 at low temperatures but remain close to bulk values at higher temperatures, changing in this manner the enthalpy of formation. However, this effect is accompanied by a high degree of disorder of the hydride phase, which acts as an extra barrier in the overall free energy change during hydrogenation of the system, partially compensating the enthalpy gain.

■ MATERIALS AND METHODS

Using a spark discharge setup previously described in ref 24, Mg−Ti nanocomposites were synthesized from the elements (Ø6.35 mm rods, 99.9+% purity, Mateck GmbH). A spark discharge between a Ti cathode placed opposite a grounded Mg anode was used to ablate material from both electrodes, and the resultant mixed metal vapor cloud was quenched rapidly to form the Mg−Ti nanocomposites. A series of 5 different batches of samples were produced, in which the electrode spacing was varied between 1 and 2 mm. The working gas was purified Ar as previously reported.[4] In this study, we concentrated on the hydrogen storage properties of two selected samples produced using an electrode spacing of 2 mm, with a mass of 5.1 and 4.5 mg, respectively, and the relationship with their structural properties. Sparks were generated at a rate of 200 Hz using a 20 nF capacitance and a charging current of 8.5 mA, for a total power input of 9.3 W. Particles were collected during 9 h runs at a rate of 0.14 mg/h on Ø47 mm PVDF membrane filters with 0.45 μm pore size (Durapore, Millipore) in a special filter holder, and transferred to an Ar filled glovebox (<0.1 ppm H_2O and O_2) for further sample preparation.

The structure of the crystalline samples was investigated by X-ray diffraction using a PANalytical X'Pert PRO diffractometer with a Cu Kα beam (λ = 1.5415 Å) operated at 40 kV and 40 mA. The samples were loaded in an Ar filled glovebox in airtight sample holders. To reduce the background due to the low amount of sample used, a silicon single crystal disk was used as a support plate. The background measured from the silicon disk and sample holder was subtracted from the X-ray diffraction patterns. Rietveld analysis was performed on the measured patterns, using the GSAS software.[25] The sizes of crystallites were calculated using the Scherrer formula and assuming a Scherrer constant of 1.

Transmission electron microscopy (TEM) studies, including energy-dispersive x-ray spectrometry (EDS), selected-area electron diffraction (SAED), and electron energy loss near-edge spectroscopy (ELNES), were performed using a FEI Tecnai TF20 electron microscope operated at 200 kV. Samples were mounted on Quantifoil microgrid carbon polymer supported on a copper grid.

Hydrogen absorption isotherms were measured using a Hy-Energy PCT Pro 2000 Sievert's apparatus. For the measurements, hydrogen gas of purity 5.0 was used. The accuracy of the pressure reading was 1%. The drift in the pressure reading is between 14 and 42 mbar within six months. With the dry scroll pump used in the setup, a base

pressure at the inlet of 5×10^{-2} mbar was achieved. Pressure–composition-isotherms (PCIs) were measured with the use of the MicroDoser attachment, and the typical size of the aliquot was 0.663 mL. The temperature of the samples, consisting of similar amounts of loosely packed powders (4.5 mg and 5.1 mg), occupying similar volumes in the MicroDoser sample space, was kept constant to within 0.5 °C during each PCI measurement.

■ RESULTS

Structural Characterization of the Mg–Ti Nanocomposites. The overall composition of the samples was studied using X-ray diffraction. The analysis of the diffraction patterns revealed that the spark discharge generated nanocomposites consist of several different crystalline phases: nanoparticles with the hexagonal Mg and Ti phases (space group $P6_3/mmc$) are present along with rock salt cubic MgO (space group $Fm\overline{3}m$), as shown by the representative example in Figure 1a. Interestingly, all samples further showed the presence of a body-centered-cubic (bcc) Mg–Ti alloy phase (space group $Im\overline{3}m$), as revealed by the presence of a dominant (110) diffraction peak at 35.1°, corresponding to a lattice parameter of 3.61 Å. Such a bcc Mg–Ti alloy with random site occupation was previously observed by Asano et al.[20,26] in $Mg_{1-y}Ti_y$ alloys (0.25 < y < 0.65) synthesized by means of ball-milling, where smaller lattice parameters near 3.42 Å were found. The presence of the face-centered cubic and hcp Mg–Ti alloy phases observed by Asano et al.[20,21] can be ruled out for the spark discharge generated nanocomposites, on the basis of our X-ray diffraction results. The presence of the bcc $Mg_{1-y}Ti_y$ alloy phase is quite remarkable, given the positive enthalpy of mixing of Mg and Ti. Unlike our previous studies,[4,5] where a set of two spark generators was used to produce nanocomposites of Mg particles interdispersed with Pd or Nb catalyst particles, the use of a Mg electrode against a Ti electrode in a single spark generator allows the formation of the Mg–Ti alloy phase, as the particles now form in a mixed metal vapor cloud. Samples generated with this electrode configuration using a spacing of 1.25 to 2 mm between the two electrodes consist in large part of the bcc Mg–Ti phase with phase fractions in the range 30–52 wt %. This demonstrates the capability of spark discharge generation to synthesize metastable Mg–Ti alloys by rapid quenching of the Mg and Ti clouds that are intermixed at an atomic scale. Such a bcc $Mg_{1-y}Ti_y$ alloy was previously also obtained after prolonged ball milling of 20–200 h of Mg and Ti powders,[20,21,26,27] for compositions reportedly in the range 0.25 < y < 0.65. The bcc Mg–Ti alloy phase stabilizes most easily near a composition of $Mg_{0.5}Ti_{0.5}$.[27] An essential difference is that, during ball milling, the size of the grains building up a micrometer-sized particle is reduced to nanoscale dimensions, whereas in the case of spark discharge, the particles themselves are nanosized as TEM indicates. This key difference has a pronounced impact on the hydrogen sorption properties of these types of samples, as shown further on.

Rietveld refinement was successfully performed on the XRD patterns, and the results are summarized in Table 1. The extracted particle sizes were found to be small for each of the phases. The size of the bcc phase Mg–Ti particles is 11 ± 2 nm. The apparent crystallite size of MgO is 3 ± 1 nm for as-prepared samples, which indicates that the MgO is present as a thin shell around the particles of Mg, as seen in our previous studies[4,5] and for Mg nanoparticles produced by inert gas condensation methods.[7–9] According to the refinement results, hexagonal Mg and Ti are present in the sample at relatively

Table 1. Particle Sizes and Phase Fractions in wt % (at %) Extracted from Rietveld Refinement of the XRD Patterns of Freshly Synthesized Mg–Ti Nanocomposites and Mg–Ti–H Nanocomposites after Hydrogen Sorption

phase	freshly prepared (R_{wp} = 2%)		after hydrogen sorption (R_{wp} = 2.8%)	
	particle size	phase fraction	particle size	phase fraction
Mg	14 ± 2 nm	10 wt % (15.0 at %)	16 ± 3 nm	13 wt % (18.8 at %)
Ti	27 ± 5 nm	9 wt % (6.9 at %)		
$Mg_{0.5}Ti_{0.5}$	11 ± 2 nm	45 wt % (45.5 at %)	8 ± 1 nm	2.2 wt % (2.1 at %)
$Mg_{1-y}Ti_yH_x{}^a$			12 ± 2 nm	26 wt % (27.4 at %)
MgH_2			21 ± 4 nm	0.8 wt % (1.1 at %)
MgO	3 ± 1 nm	36 wt % (32.6 at %)	5 ± 1 nm	58 wt % (50.6 at %)

^{a}The weight fraction was calculated using a composition of $Mg_{0.7}Ti_{0.3}H_2$.

small fractions of 10 and 9 wt %, respectively. The sample is dominated by a high fraction of about 45 wt % of the cubic Mg–Ti alloy. The fractions obtained from the XRD measurements point to an overall metal fraction of Mg of 70 at % and of Ti of 30 at %. This result is very similar to the fractions obtained from ICP-OES and TEM-EDS, as it is summarized in Table 2. Both XRD and ICP-OES characterize a bulk average of

Table 2. Mg and Ti Fraction of Metal Elements Present, As Obtained through XRD, ICP-OES, and EDS for the As-Produced Mg–Ti nanocomposites

element	XRD at %	ICP-OES at %	TEM-EDS at %
Mg	70	67	69
Ti	30	33	31

the sample, while TEM-EDS gives very local information about the sample composition, obtained for several parts of the sample. Since the same composition is obtained from both global average and local measurements, one may conclude that the composition is uniform throughout the as-prepared sample. Thus, spark discharge generation not only allows the mixture of metals on a very small scale but also as a uniform mixture.

The sample was subjected to several cycles of hydrogen loading and unloading at temperatures up to 300 °C in a Sievert's setup. After the cycling, XRD was used to determine the resulting phases in the partially loaded state (Figure 1b). A noteworthy fact is the disappearance of the crystalline Ti phase and the appearance of a face-centered-cubic (fcc) $Mg_{1-y}Ti_yH_x$ phase similar to fluorite TiH_2 with an expanded lattice parameter. Such a fluorite cubic $Mg_{1-y}Ti_yH_x$ phase was previously observed upon hydrogenation of hcp $Mg_{1-y}Ti_y$ thin films for Ti-fractions larger than ~15 at %, where it could be attributed to the stabilizing presence of nanoscale fluorite TiH_2 domains. For these thin films, the cubic fluorite $Mg_{1-y}Ti_yH_x$ phase showed a substantially faster hydrogen sorption kinetics than the rutile $Mg_{1-y}Ti_yH_2$ phase which stabilizes at low Ti-fractions.[18,16] Furthermore, studies on ball-milled Mg–Ti powders also revealed the presence of the fluorite fcc $Mg_{1-y}Ti_yH_x$ phase upon hydrogenation.[21,22] In the Rietveld analysis, we obtained a very similar XRD pattern for the
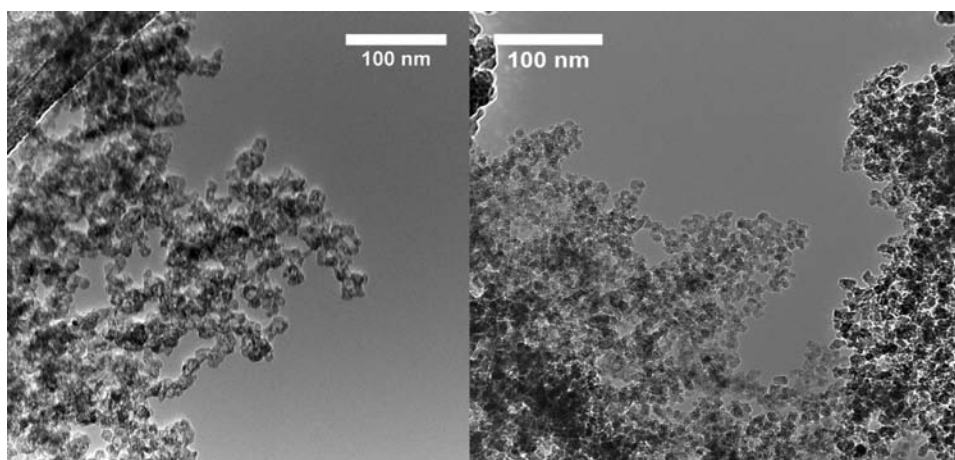
7893

dx.doi.org/10.1021/ja3123416 | *J. Am. Chem. Soc.* 2013, 135, 7891–7900

Figure 2. Transmission electron micrographs of spark discharge generated Mg−Ti nanocomposites. Left: As produced. Right: After partial hydrogen loading (see text).
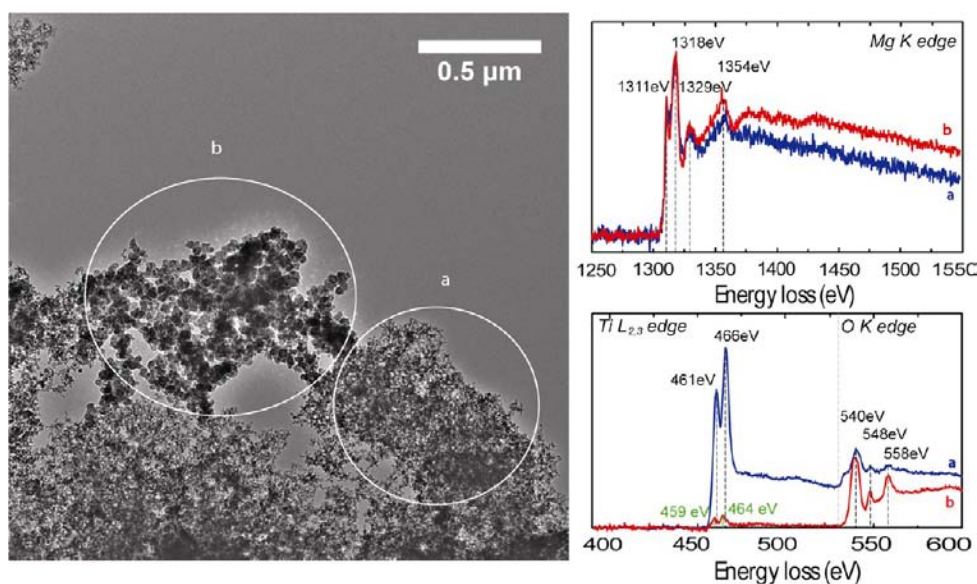

Figure 3. Morphology and local composition of spark discharge generated Mg−Ti nanocomposites after (partial) hydrogen loading. Left: TEM image exhibiting regions a and b with the two types of morphology present in the sample. Right: Electron energy loss near-edge spectra for the regions a and b depicted in the TEM-image: Mg K edge (top) and Ti $L_{2,3}$ edge together with O K edge (bottom).

$Mg_{1-y}Ti_yH_x$ phase (see Figure 1b, bottom) as obtained in these studies.[21,22] Rietveld refinement was performed with a R_{wp} of 2.8%, and the results are summarized in Table 1. Significantly, only a very minor fraction of the sample had transformed to the common rutile MgH_2 phase, as can be seen from the very weak intensities of the characteristic diffraction peaks at 54° and 28° (Figure 1b), showing the large preference for a transformation into the fluorite cubic $Mg_{1-y}Ti_yH_x$ phase upon hydrogenation under the applied conditions. The lattice parameter obtained for the $Mg_{1-y}Ti_yH_x$ phase is $a = 4.44$ Å, a visible increase from the typical value of 4.36 Å for TiH_2. From studies on Mg−Ti thin films[16] but also on ball milled Mg−Ti systems,[22] it is known that the presence of Mg in TiH_2 indeed leads to an increase in unit cell. The lattice parameters obtained for the cubic Mg−Ti−H phase obtained by means of ball-milling, with values of 4.49 Å found for the $Mg_{0.42}Ti_{0.58}H_{1.77}$ phase reported by Asano et al.[21] and of 4.47 Å found for the $Mg_{0.5}Ti_{0.5}H_x$ phase by Rousselot et al.,[22] are quite close to the lattice parameter of the fcc Mg−Ti−H phase observed here. Although $Mg_{1-y}Ti_yH_2$

thin films obey Vegard's law that predicts a linear increase in lattice parameter with Mg fraction, in the present study it is not possible to reliably extract the exact composition of the cubic $Mg_{1-y}Ti_yH_x$ phase due to the uncertainty in the amount of hydrogen present and the large lattice expansion it can generate. Assuming a maximum hydrogen uptake, one may estimate a lower limit on the Mg-fraction of the $Mg_{1-y}Ti_yH_x$ of 20%, which would indicate a composition of $Mg_{0.2}Ti_{0.8}H_2$. However, because of the uncertainty in the hydrogen fraction, the actual Mg fraction can be significantly higher. It is interesting to compare the observed cubic fluorite structure of the $Mg_{1-y}Ti_yH_x$ phase with the structure of the cubic Mg_7TiH_{16} compound synthesized by high pressure methods.[23,28] The latter Mg_7TiH_{16} compound showed an ordered Mg−Ti metal sublattice superstructure[23,28] with the cubic Ca_7Ge structure ($Fm\bar{3}m$, No. 225), involving a doubling of the cubic unit cell in all three space dimensions. In our electron diffraction images we did not see the low-angle diffraction peaks characteristic for the superstructure. Also, the lattice parameter

of the Mg_7TiH_{16} compound of 4.782 Å for the substructure is significantly different from the lattice parameter of 4.44 Å for the fluorite cubic $Mg_{1-y}Ti_yH_x$ nanocomposites observed in our XRD data, excluding the formation of the high-pressure Mg_7TiH_{16} phase for the hydrogenated spark discharge generated samples.

The crystallites of the $Mg_{1-y}Ti_yH_x$ phase are small, 12 ± 2 nm as determined from peak broadening in the XRD pattern. Though the fraction of the MgO oxide is increased after hydrogen cycling, the average size of MgO crystallites (or shells) of about 5 ± 1 nm remains quite small.

During hydrogen cycling, the cubic Mg−Ti−H metal hydride most likely transforms into the common hcp Mg−Ti phase upon desorption. For example, in studies on Mg−Ti films[14,29] where the fluorite type hydride is created upon hydrogenation, the extraction of hydrogen results in a transformation back to the original hexagonal Mg−Ti phase. However, in a study of the structural transformations upon hydrogen cycling of a metastable hcp Mg−Ti alloy obtained by means of ball-milling, Rousselot et al.[30] found that, in the first cycle, a stabilization to a Mg−TiH_x fluorite fcc phase occurred, and the extraction of hydrogen was only accompanied by a change in the lattice parameter but not by a change in the symmetry.

In order to gain a better understanding of the changes that occur as a result of the hydrogenation and corresponding heating treatments under exposure to hydrogen, transmission electron microscopy was applied to investigate the morphology and the local composition of the sample. The general aspect of the as-prepared sample is of a nanomaterial of a very porous nature (Figure 2, left). Particles with a close to a spherical shape of about 10−20 nm in diameter are organized in fractal-like dendritic structures. Small area electron diffraction showed that even locally the samples are of crystalline nature, but the small size of the crystallites gives rise to broad and diffuse diffraction rings. This result is consistent with the analysis of the XRD patterns. At the edges of the primary particles, a thin shell of a different density can be identified as MgO. The MgO fraction increases with the repeated hydrogen loading and unloading due to traces of oxygen present in the hydrogen gas. The sintering of the particles is more pronounced in the MgO-rich regions as it will be explained further on.

After six hydrogen loading and unloading cycles, the main features of the initial morphology are mostly preserved in the partially loaded sample, as it can be seen in Figure 2, right. However, a more detailed analysis reveals the appearance of local nonuniformity in the morphology and composition of the sample after the hydrogen cycling. In the TEM image shown in Figure 3, the two representative morphologies of the sample after cycling are depicted. Region a has a morphology which is very similar to that of the as-prepared sample, with a metal composition close to 70 at % of Mg and 30 at % of Ti. Particles in this area maintain a small size and the porous aspect. Region b is formed of agglomerated spherical particles of significantly larger sizes in the range 50−100 nm. The ratio between Mg and Ti is here largely increased to 96.7 at % Mg to 3.3 at % Ti. A high fraction of O is detected using EDS, leading to the conclusion that a significant fraction of the Mg in region b is oxidized to MgO.

An electron energy loss near-edge spectroscopy (ELNES) study of the Mg K edge, the O K edge, and the Ti $L_{2,3}$ edge was performed in both regions a and b, which provided key information on the local composition and chemical binding state of the Mg and Ti. The positions of these element specific

edges in the ELNES spectrum depend on the binding energy of the core electrons, which shifts as a function of the valence state of the element and thus provides insights into its local chemical environment. The structure of the edges depends on the chemical environment of the element and the conduction (upper valence) electron energy density-of-states.

In Figure 3, the Mg K edge spectra obtained in region a and in region b both reveal the presence of the two characteristic main peaks, at 1311 and 1318 eV, corresponding to the binding energy of the Mg 1s electrons, and lower intensity broader peaks at 1329 and 1354 eV. The lowest energy peak at 1311 eV is clearly shifted from the value of about 1304 eV for Mg metal determined by X-ray absorption spectroscopy (XAS)[31] and X-ray photoelectron spectroscopy (XPS),[32] but is much closer to the value of about 1310 eV for Mg in MgO indicated by XAS[31] and XPS.[32] The effect of a transition metal on the Mg ionization edge, on the other hand, is a shift toward lower energies as reported by Farangis et al.[31] Further, XAS measurements have shown that a positive shift of 2.5 eV can be expected in the hydride state.[31] The position of 1311 eV of our measured ionization edge is the result of a combination of the contributions of Mg present in MgO, MgH_2, and metallic Mg, as revealed by the XRD spectra. Clearly, oxidation plays a role in both regions. The coordination of Mg is revealed by the peaks in the backscattered electron regions at 1329 and 1354 eV. Qualitatively, the higher the intensity of the peaks in this region, the stronger the interaction of the backscattered electrons to the atoms coordinated around Mg. Thus, the relatively high intensity of the peaks at 1329 and 1354 eV measured in region b suggests that O atoms are dominant as nearest neighbors, whereas the low intensity of the peaks in the spectrum measured in region a indicates that in that region H atoms as nearest neighbors and also a metallic Mg or Mg−Ti environment are important. This strong difference in oxidation of the two areas is supported by the much stronger O K edge peaks near 540 eV observed for region b, which show that MgO is predominantly present in region b. The peak structure for the O K edge for region *b* is indeed very similar to that of crystalline MgO,[33] exhibiting characteristic oxygen nearest neighbor and oxygen next nearest neighbor peaks at 558 and 548 eV, respectively.[33]

The state of the Ti can be deduced from the $L_{2,3}$ excitation edge spectrum, which features two sharp peaks representative for the electronic transitions $2p_{1/2}$−3d (L_2) and $2p_{3/2}$−3d (L_3) at 459 and 464 eV, respectively, as it can be seen in Figure 3 (right) for the two regions a and b. These peaks correspond to two edges arising from the spin−orbit coupling of the p orbitals. The $L_{2,3}$ edge of transition metals is typically used to determine their oxidation state. Here, the edge positions observed for region b are close to the expected values of 458 and 463 eV[34] for Ti metal, suggesting that the Ti in region b is in the metallic form. The much lower intensity of the Ti $L_{2,3}$ edge in region b is directly related to the very small fraction of Ti present in this region of about 3.3 at % determined by EDS. Region a, on the other hand, presents a chemical shift of 2 eV compared to the spectrum of region b, which we attribute to the presence of TiH_2 (possibly including a partial Mg surrounding of the Ti, such as in the $Mg_{1-y}Ti_yH_2$ phase). Indeed, in their X-ray absorption spectroscopy studies of Mg−Ti thin films, Farangis et al.[31,35] report a small positive chemical shift for TiH_2 as compared to Ti metal.

Apart from the analysis of the chemical shift of the ionization edges, the oxidation state may also be determined from the

ratio between the integrated areas of the L_2 and L_3 edges.[36,37] In our study, the ratio was calculated for both a freshly prepared sample and the hydrogen-exposed sample. The ratio for the freshly prepared sample is the same as the one calculated for region b of the hydrogen-exposed sample, implying that the oxidation state of Ti in the fresh sample is the same as in region b and Ti is in its metallic form. The ratio calculated for region a is lower than that for region b, suggesting Ti is in a different oxidation state, most likely as TiH_2 or TiO_2. The latter is not likely, however, since in the case of transition metal oxides, backscattering from oxygen nearest neighbors would give rise to a prominent and broad peak at about 40 eV from the ionization edge.[33] In both spectra of the Ti edge, this feature is not present, indicating the absence of TiO_2 in the sample. This result, together with the observation of the chemical shift and the absence of Ti metal from the XRD patterns, strongly suggests the presence of Ti mainly as in its hydride form in region a and as Ti metal (in small amounts) in region b. Interestingly, Ti is prevented from oxidizing in both regions since the Mg acts as a strong scavenger for the oxygen, as evidenced by the formation of MgO.

An interesting fact is that the hexagonal Mg retains its nanostructure after hydrogen sorption, with an average small size of ∼16 nm as deduced from XRD (Table 1). In region a, this is likely related to the proximity of the fluorite cubic Mg−TiH_x particles, which may act as a grain refiner for hcp-Mg particles, similar to the grain refinement activity of TiH_2 reported for ball milled Mg−Ti powders,[38,39] induced by a favorable lattice matching for specific hcp-Mg//f-Mg−TiH_x interfaces.[38] Moreover, the results obtained from the ELNES analysis complement the findings from the XRD patterns, and infer that region b consists primarily of oxidized Mg (i.e., MgO). The high fraction of MgO found in XRD can then be directly related to its high concentration in areas similar to region b. However, region b may further contain nanosized Mg particles enclosed by MgO shells. In the hydrogen cycling experiments discussed in the following section, the mixed Mg−Ti areas of the sample such as region a form the main active phase, while region b that mainly contains MgO is seen as inert, except in the high hydrogen pressure−high temperature range where Mg nanoparticles confined by MgO shells can be hydrogenated.

In short, region b is characterized by larger agglomerated particles about 50−100 nm in size, mainly consisting of MgO domains, and further containing a minor fraction of Ti metal nanoparticles and likely also Mg/MgO core/shell nanoparticles. Region a is characterized by much smaller particle sizes preserved by grain refinement, with a similar dendritic morphology as the as-prepared sample. It consists mainly of fluorite cubic $Mg_{1-y}Ti_yH_x$ nanoparticles; further, TiH_2 and hexagonal Mg nanoparticles are likely present, leading to an overall metal composition of 70 at % Mg and 30 at % Ti. MgO is present in much smaller quantities in region a than observed in region b, mainly in the form of a shell surrounding the nanoparticles.

Hydrogen Storage Properties of the Mg−Ti Nanocomposites. As stated in the Introduction, the capability of a material to react with hydrogen is greatly influenced by the enthalpy of formation of the hydride. In the case of bulk MgH_2, the enthalpy of formation is −75 kJ/mol H_2.[40] For a practical use of a metal hydride as a viable hydrogen storage system, an enthalpy of formation of about −40 kJ/mol H_2 is often desired to achieve equilibrium pressures of the order of 1 bar near

room temperature.[1,2] Pressure−composition-isotherms (PCIs) obtained for the Mg−TiH_x nanocomposites are shown in Figure 4. The hydrogen absorption rates at the start of each
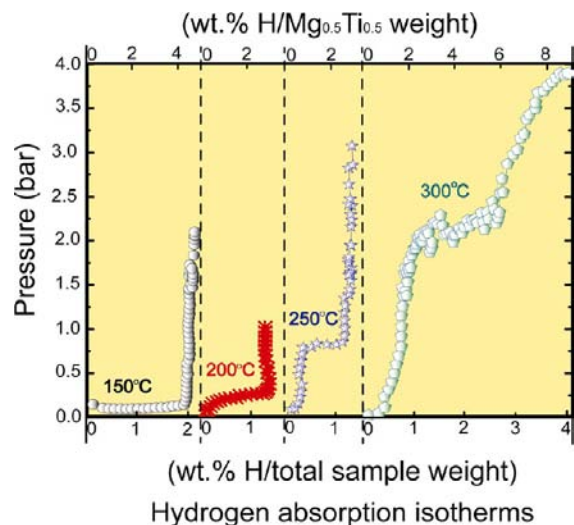

Figure 4. Hydrogen absorption isotherms for Mg−Ti nanocomposites measured at 150, 200, 250, and 300 °C, subsequently. The amount of hydrogen absorbed is expressed in weight %, both as a fraction of the weight of the sample (bottom axis) and as a fraction of the weight of the bcc Mg−Ti alloy phase initially present in the sample (top axis).

absorption step on the plateau were in the range ∼0.015−0.035 wt %/h {for $[(\Delta p)/(p_{eq})] = [(p_0 - p_{eq})/(p_{eq})] \sim 0.02-0.22$ at $t = 0$} and the plateau pressures were approached with rate constants k in the range ∼0.4−2.5 h^{-1}, i.e., of a similar magnitude as found in a previous study on the hydrogen sorption kinetics of spark discharge generated MgH_2 nanoparticles catalyzed by NbO_x or Pd nanoparticles.[5] The concentration of hydrogen in the sample is given as a weight percentage of the total mass of the sample. Because the sample contains also MgO and apparently unreactive Mg particles, the hydrogen content is also calculated as a weight percentage of the active Mg−Ti fraction of the sample associated with the initially present bcc Mg−Ti alloy phase identified in the corresponding XRD pattern. It should be noted, however, that also the initially present Ti phase is consumed upon hydrogen loading, and may participate in the formation of the $Mg_{1-y}Ti_yH_x$ phase. Possibly, it could further lead to the formation of very small TiH_2 domains, giving rise to broad peaks in the X-ray diffraction pattern[38,41] which are hard to discriminate against background, especially with small amounts of sample.

The PCIs, measured subsequently at 150, 200, 250, and 300 °C, each exhibit a region where the pressure remains constant while the hydrogen content of the sample increases. This region is commonly defined as the coexistence (or equilibrium) plateau. The plateau pressures were determined at the midpoint of each plateau. Interestingly, the plateau pressures are larger than the equilibrium pressure of bulk MgH_2 and ball milled MgH_2 powders in the full temperature range between 150 and 300 °C. The strongest effect appears at 150 °C when a plateau pressure of p_{eq} = 96 mbar was measured compared to the equilibrium pressure of p_{eq} = 5.2 mbar for bulk (or ball milled) MgH_2.

These plateaus cannot be attributed to either hydrogenation of Mg or Ti nanoparticles. The former remain seemingly unloaded after the Sievert's measurements as deduced from the

XRD patterns of the as-prepared and loaded sample (see Table 1). The pressure of only ~1.5 mbar at the highest temperature of 300 °C required for the hydrogenation of bulk metallic Ti to titanium hydride with a composition of $TiH_{\sim1.9}$ (ref 42) on the other hand is far lower than the observed plateau pressures.

Therefore, the origin of the plateaus must be linked to the transformation of the $Mg-Ti$ to $Mg-TiH_x$ nanocomposite phases as found in the active areas of the sample similar to region a. At the highest temperatures of 250 and 300 °C, a low pressure range up to a hydrogen fraction about 0.4 wt % is visible, which could be due to the storage of hydrogen in TiH_2, since a low pressure of about 1.5 mbar is sufficient to reach a composition of $TiH_{\sim1.9}$ in the δ-phase of TiH_x at 300 °C (ref 42). At 300 °C, three ranges are visible in the pressure-composition-isotherm of Figure 4, where a high pressure range starts at the end of the equilibrium plateau, i.e., beyond 2.7 wt % loading, characterized by a gradual increase in pressure with hydrogen content. This behavior could correspond to the transformation to destabilized rutile MgH_2 of hcp-Mg particles confined within a MgO shell. Upon removal of hydrogen pressure, such destabilized MgH_2 areas might have released their hydrogen before the XRD analysis was performed. An interesting alternative possibility is that the H is inserted in the hexagonal Mg phase which cannot convert to the rutile MgH_2 structure, as observed in a previous study by Mulder et al.,[38] due to the destabilization of the rutile MgH_2 phase by, e.g., the presence of the MgO shells. The lattice parameters of such a $Mg(H_x)$ solution phase were found to hardly change for compositions up to $MgH_{0.5}$.[38] This would also explain why the XRD analysis performed still shows the Mg phase.

For a first order hydrogenation reaction, a van't Hoff analysis can be made for the determination of the enthalpy and entropy of the hydrogenation reaction. Since the pressure and temperature remain constant at the plateau, the chemical potential of both the hydrogen gas and the coexisting metal and metal hydride solid phases during the transformation is constant for the width of the plateau. The natural logarithm of the equilibrium pressure plotted against the reciprocal temperature gives a line according to the van't Hoff equation, $\ln[(p_{eq})/(p_0)] = (\Delta H/RT) - (\Delta S/R)$, as it can be seen in Figure 5. The enthalpy change for the hydrogenation reaction calculated from the slope of curve a in Figure 5 is −45 kJ/molH₂. This value is much less negative than any enthalpy of
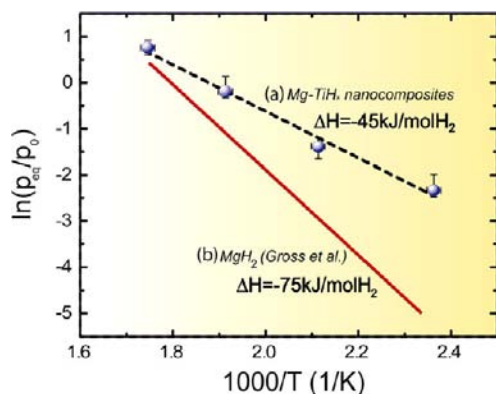
formation reported so far for $Mg-TiH_x$ nanocomposites. The obtained entropy of the reaction is 84 J/K mol H₂. Reduced values for the enthalpy and entropy, of, respectively, −54 ± 3 kJ/mol H₂ and 99 ± 6 J/K mol H₂, were also obtained for the second sample (see Figure 6). Lu et al.[43,44] found a reduced
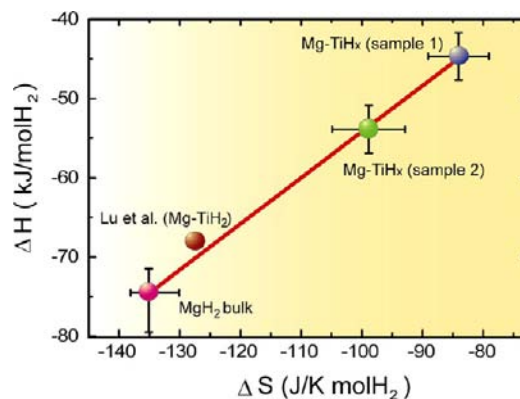

Figure 6. Linear relation between enthalpy and entropy as obtained for Mg−Ti nanocomposite samples compared to literature values for bulk MgH_2.

enthalpy of formation for the $MgH_2-0.1TiH_2$ system of −68 kJ/mol H₂, but the effect is much milder for such ball milled $Mg-0.1TiH_2$ nanocomposites with a grain size of 5−10 nm. Using hydrogenography,[45] a combinatorial technique for fast screening of the thermodynamics of hydrogenation of thin metal films, Gremaud et al.[45,46] determined the formation enthalpies of more than 500 compositions of $Mg_{1-y}Ti_y$ (0.60 < y <0.89) in a single experiment. The enthalpy of formation of the fluorite cubic $Mg_{1-y}Ti_yH_x$ phase was observed to be in the range −65 to −58 kJ/mol H₂ in the composition range 0.65 < y <0.89, i.e., rather close to that of rutile MgH_2 films (−60.7 kJ/mol H₂).[47] The less negative enthalpy of formation for rutile MgH_2 films relative to that of bulk MgH_2 is caused by clamping of the film to the substrate during hydrogenation, leading to a compressive strain of the metal hydride film and a destabilization of the metal hydride phase.

The origin of this strong deviation of the reaction enthalpy, entropy, and the low temperature plateau pressures from the values expected for the hydrogenation reaction of hexagonal Mg to the common rutile MgH_2 phase should be sought in the nanosize and finely intermixed character of the Mg−Ti−H nanocomposites produced by spark discharge generation. First of all, it is well-known that, at the nanoscale, the thermodynamic properties of the Mg-to-MgH_2 hydrogenation reaction may change dramatically because of the modified structure of the nanocrystals and the dominant contribution of the surface (or interface) structure and local bond lengths at the smallest sizes. Further, the hydrogenation involves the formation of a metastable fluorite cubic $Mg_{1-y}Ti_yH_2$ phase with a different chemical binding as for the rutile MgH_2 phase, which may lead to a changed reaction enthalpy. Finally, since EXAFS[16] and positron annihilation studies[48] indicate that thin films exhibiting an X-ray coherent fluorite cubic $Mg_{1-y}Ti_yH_x$ phase are in fact chemically segregated into MgH_2 and TiH_2 domains at length scales of the order of ~1 nm, it can be expected that the Mg−Ti−H nanocomposites studied here consist of similar locally segregated coherent MgH_2 and TiH_2 domains. For such nanocomposites, interface energies and elastic effects between attached MgH_2 (or Mg) and TiH_2

Figure 5. (a) Van't Hoff plot for the Mg−Ti nanocomposites obtained from the plateau pressures in the P−C−T measurements. The dashed line represents the linear best-fit to the data. (b) Van't Hoff plot for bulk MgH_2 as measured by Gross et al.[40]

nanodomains (for example, induced by strains imposed on the crystal lattice) should be taken into account as they may strongly affect the thermodynamic properties. Further, the formation of excess free volume and defects may influence the thermodynamics. The chemical transformations are then accompanied in an essential way by rearrangements in the structure. The microstructure and nanostructure of the sample will consequently play an important role in the established thermodynamic equilibrium state of the sample. Below we will discuss the possible role of each of these mechanisms in the observed strong changes in the reaction enthalpy, entropy, and the low temperature equilibrium pressures for the Mg−Ti−H nanocomposites.

Ab initio studies by Wagemans et al.[49] demonstrated that the enthalpy of hydrogenation for the Mg-to-MgH$_2$ hydrogenation reaction is clearly reduced for very small Mg nanoparticles due to the modified crystal structure and local binding in the surface area of the particles, leading to reaction enthalpies of the order of −63 kJ/mol H$_2$ at a diameter of 1.8 nm. However, the reaction enthalpy only changes significantly for particle diameters below about 3 nm, making this mechanism rather improbable for the studied Mg−Ti−H nanocomposites with primary particle sizes which are about 5 times larger.

A second factor which may lead to modified thermodynamics is the formation of a coherent fluorite Mg$_y$Ti$_{1-y}$H$_x$ hydride as inferred from our X-ray diffraction study. Theoretical studies[50−52] predicted substantial thermodynamic changes for such a cubic fluorite Mg$_y$Ti$_{1-y}$H$_x$ hydride phase relative to the rutile Mg$_y$Ti$_{1-y}$H$_x$ phase. It is expected that a stabilization of the fluorite Mg$_y$Ti$_{1-y}$H$_x$ hydride occurs below a critical composition of $y \sim 0.8−0.9$.[50] The calculated enthalpy difference between the fluorite Mg$_{0.875}$Ti$_{0.125}$H$_2$ and the rutile MgH$_2$ phase is about +10 kJ/mol H$_2$.[50] Therefore, this mechanism could provide a significant contribution to the observed increased enthalpy of formation. However, it should be noted that the observed Mg fraction is clearly lower than $y \sim 0.875$, and on the basis of the calculations, the destabilizing effect will be canceled for a Mg fraction of ∼0.7. The latter is close to the actual average concentration observed in region a by TEM-EDS.

Mg and Ti have a strong tendency to phase segregate as they are essentially immiscible elements. Therefore, similar to the chemical segregation into Mg and Ti nanodomains with a typical domain size well below 10 nm observed for X-ray coherent Mg−Ti thin films, the presence of coherent neighboring Mg and Ti domains should be considered here as well. The presence of an interface will affect the enthalpy of formation of hydrogenated Mg−TiH$_x$ nanocomposites, since the local binding at the interface will modify the energy of the system. Mooij et al.[53] have experimentally determined the magnitude of the difference in the interface energy of the hcp Mg(0002)//TiH$_2$(111) and rutile MgH$_2$(110)//TiH$_2$(111) systems in a series of P−C−T experiments on Mg//Ti multilayer systems with varying layer thicknesses. The interface model applied in that study could well explain the observed increase in the equilibrium pressures and presence of hysteresis, with an extracted interface energy difference close to that obtained from the ab initio calculations. However, using the model of Mooij et al.[53] for the Mg−TiH$_x$ nanocomposite with a typical particle size of ∼10−20 nm studied here, the effect of the interface energy on the equilibrium pressure is estimated to be relatively small, about 4.5 kJ/molH$_2$ for particles with a radius of 10 nm. This increase in enthalpy is much lower than the total change in enthalpy observed in our materials. Also, the

increase in equilibrium pressure by a factor of ∼10 (as observed in our study at low temperature) was reached only for very thin multilayer films with a layer thickness of about 2 nm or less.[53] This indicates that the mechanism leading to the observed higher absorption equilibrium pressures for the spark discharge generated nanocomposites is more complex.

A fourth factor which may affect the enthalpy of formation of MgH$_2$, proposed by Hao and Sholl,[54] involves the induced strain imposed on the crystal lattice for hcp Mg and rutile MgH$_2$ when stacked as epitaxial thin layers on TiH$_2$(111) surfaces. The ab initio calculations by Hao and Sholl predicted a significant reduction of the enthalpy of formation of MgH$_2$ of up to 12 kJ/mol H$_2$ for the smallest layer thicknesses by such a strain-induced change of the thermodynamics of the reaction.[54] Our EELS analysis of the nanocomposites is consistent with the presence of Mg domains in close proximity of TiH$_2$ domains, supporting such a mechanism. However, the estimated size of the changes in the enthalpy of formation indicates that the interface energy and the lattice strain at the Mg and TiH$_2$ boundaries can only partially explain the magnitude of the reduced enthalpy of formation and increased plateau pressures for the spark discharge generated Mg$_y$Ti$_{1-y}$H$_x$ nanocomposites.

It is interesting to note that a modified enthalpy and entropy were also observed for MgH$_2$ nanoparticles (<3 nm) nanoconfined in a carbon scaffold investigated by Zhao-Karger et al.[55] A less negative enthalpy of −63.8 ± 0.5 kJ/mol H$_2$ and reduced reaction entropy of 117.2 ± 0.8 J/K mol H$_2$ was observed. These differences with respect to bulk MgH$_2$ are smaller than for the present case of Mg$_y$Ti$_{1-y}$H$_x$ nanocomposites, but again show a trend in the same direction in the $\Delta H−\Delta S$ diagram presented in Figure 6. The enthalpy change was attributed to the effects of small particle size and of strain imposed by the carbon scaffold, but a mechanism for the entropy change was not provided. As discussed above, the effect of strain, exerted by a neighboring TiH$_2$ local environment (instead of a carbon scaffold) on Mg/MgH$_2$ nanoparticles, can also play an important role for the Mg$_y$Ti$_{1-y}$H$_x$ nanocomposites.

We further considered the model by Berube et al.,[56−58] based on a destabilization of the hydride phase due to significant local distortions of the bulk equilibrium crystal lattice by the presence of, e.g., grain boundaries, vacancies, or dislocations. The deformation of the crystalline structure by such defects is included in the equation of state as a generic term: the excess volume, which represents the ratio between the actual (expanded) volume and the equilibrium volume. According to this model, an excess volume of about 10% would be enough to account for the observed large enthalpy change of about 30 kJ/mol H$_2$. Moreover, the Berube model[56−58] also predicts an increase in the entropy in the distorted regions, and, consequently, a reduction in the entropy of the hydrogenation reaction compared to the bulk values. In our study, the entropy is observed to change to 84 ± 5 J/K mol H$_2$, modifying the free energy of the system by acting as a barrier and thus partially compensating for the effects of the decreased enthalpy formation on the equilibrium pressures and chemical potentials. It thus appears that a decrease of the enthalpy of formation is accompanied by an increased disorder of the hydride lattice, quite similar to what has been observed for ball-milled MgH$_2$ powders using a TiF$_3$ catalyst by Mulder et al.[38] Moreover, Figure 6 shows that the variation in enthalpy and entropy of formation follows a linear behavior, similar to what was observed by Mulder et al.[38] In the latter study, however, the largest effects were seen in the Mg(H$_x$) solution phase in a wide

range of hydrogen concentrations. The alteration of ΔS compared to bulk Mg−MgH$_2$ was subsequently described as resulting from the remaining large configurational entropy associated with the partial H site occupations.[38] The range of this solution phase for the ball-milled TiF$_3$-catalyzed MgH$_2$ powders was expanded in a remarkable way up to hydrogen concentrations of $x \sim 0.5$, induced by the presence of abundant interfaces such as the Mg(0002)//TiH$_2$(111) interface. Here, we extracted the enthalpy and entropy of the hydrogenation reaction from clearly discernible equilibrium plateaus in the full pressure−composition isotherms that are representative for the entire active sample.

We note that the hydrogen desorption of the sample was too slow in the low temperature range studied to quantify the hysteresis between the absorption and desorption isotherms, except at the highest temperature of 300 °C, where the hydrogen desorption rate at the plateau was typically about 70% of the hydrogen absorption rate at 300 °C. At this temperature, a hydrogen desorption plateau pressure of 1.4 bar was reached, resulting in a hysteresis of ∼0.6 bar. At lower temperatures, hardly any pressure increase could be seen during desorption steps of typically 3 h in measurements of the desorption PCI at the plateau. Hydrogen desorption could only effectively be promoted by desorption into a vacuum for prolonged times of the order of 50 h. The slowness of hydrogen desorption is, apart from the low temperatures involved, likely also due to the presence of MgO shells surrounding the Mg−Ti−H nanoparticles.[4] The van't Hoff plot derived in this study is therefore representative for the hydrogenation reaction only. The hydrogen desorption is likely accompanied with a hysteresis for all studied temperatures, known to exist also for ball milled MgH$_2$ nanopowders[59,60] and thin film systems.[53] Such a hysteresis may be enhanced by plastic deformation which itself may lead to higher apparent equilibrium pressures for the hydrogenation reaction as well.[53]

Although the model proposed by Berube et al.[56−58] predicts the most severe enthalpy changes, comparable in size with the observations, we note that XRD and TEM analysis both confirmed the crystalline structure of the sample. The complexity of the Mg−Ti nanocomposite samples in terms of composition, morphology, and crystallinity in fact points to a combination of the different mechanisms discussed above, leading to the pronounced reduction in enthalpy of formation which underlines the great promise for Mg−TiH$_x$ nanocomposites as hydrogen storage materials. Nonequilibrium synthesis methods such as spark discharge generation open up a way to tailor finely interdispersed nanocomposites and new types of nanoalloys with desirable hydrogen storage properties.

CONCLUSIONS

Spark discharge generation synthesis has proven to be very attractive for producing finely intermixed composites of Mg−Ti nanoparticles. The mixture of the two metals is uniform across the sample, and it corresponds to the targeted 70 at % Mg and 30 at % Ti as determined by three different analysis methods, XRD, TEM-EDS, and ICP-OES. A direct product of the spark discharge synthesis is a metastable bcc Mg−Ti alloy phase which was identified in the XRD patterns. The hydrogenation reaction of this phase leads to the formation of the fluorite Mg−TiH$_x$ hydride phase instead of the commonly observed rutile MgH$_2$ phase, and which exhibits promising hydrogen storage properties. This opens up a way for up-scaling the production of this interesting hydrogen storage material

previously identified in thin films. A much less negative enthalpy of formation of the hydride compared with bulk MgH$_2$ is observed. Its origin stems from the nanostructured character of the finely intermixed composite with primary particle sizes in the range 10−20 nm. In particular, mechanisms involving lattice strains, the presence of interfaces between coherent Mg and TiH$_2$ nanodomains, the presence of hydrogen vacancies, and the formation of excess free volume due to local deformations of the material are plausible causes for the observed strongly modified thermodynamics. Further, the formation of the metastable fluorite Mg−TiH$_x$ hydride phase could contribute to the observed reduction in the enthalpy of formation. The modified enthalpy leads to largely increased plateau pressures at low temperatures. At the same time, the entropy of the hydrogenation reaction is also lowered to 84 ± 5 J/K mol H$_2$ due to an increase in the degree of disorder of the hydride phase, partially compensating the effects of the reduced enthalpy on the plateau pressures. The present study represents an important step in the challenge to find Mg-based hydrogen storage materials with a suitable thermodynamics of hydrogen sorption. Further investigations on the interplay of microstructure and chemical composition could reveal the detailed mechanisms of the enthalpy reduction observed for these Mg−TiH$_x$ nanocomposites, which show great promise as hydrogen storage materials.

AUTHOR INFORMATION

Corresponding Author

s.w.h.eijt@tudelft.nl

Notes

The authors declare no competing financial interest.

REFERENCES

(1) Schlapbach, L.; Züttel, A. *Nature* **2001**, *414* (6861), 353−358.
(2) Züttel, A. *Mater. Today* **2003**, *6* (9), 24−33.
(3) Liang, G.; Huot, J.; Boily, S.; Van Neste, A.; Schulz, R. *J. Alloys Compd.* **1999**, *291*, 295−299.
(4) Vons, V. A.; Anastasopol, A.; Legerstee, W. J.; Mulder, F. M.; Eijt, S. W. H.; Schmidt-Ott, A. *Acta Mater.* **2011**, *59* (8), 3070−3080.
(5) Anastasopol, A.; Pfeiffer, T. V.; Schmidt-Ott, A.; Mulder, F. M.; Eijt, S. W. H. *Appl. Phys. Lett.* **2011**, *99* (19), 194103.
(6) Tabrizi, N.; Ullmann, M.; Vons, V.; Lafont, U.; Schmidt-Ott, A. *J. Nanopart. Res.* **2009**, *11* (2), 315−332.
(7) Krishnan, G.; Kooi, B. J.; Palasantzas, G.; Pivak, Y.; Dam, B. *J. Appl. Phys.* **2010**, *107*, 052504.
(8) Callini, E.; Pasquini, L.; Piscopiello, E.; Montone, A.; Antisari, M. V.; Bonetti, E. *Appl. Phys. Lett.* **2009**, *94*, 221905.
(9) Pasquini, L.; Montone, A.; Callini, E.; Antisari, M. V.; Bonetti, E. *Appl. Phys. Lett.* **2011**, *99*, 021911.
(10) de Jongh, P. E.; Wagemans, R. W. P.; Eggenhuisen, T. M.; Dauvillier, B. S.; Radstake, P. B.; Meeldijk, J. D.; Geus, J. W.; de Jong, K. P. *Chem. Mater.* **2007**, *19* (24), 6052−6057.
(11) Bogerd, R.; Adelhelm, P.; Meeldijk, J. D.; de Jong, K. P.; de Jongh, P. E. *Nanotechnology* **2009**, *20*, 204019.
(12) Zlotea, C.; Chevalier-César, C.; Léonel, E.; Leroy, E.; Cuevas, F.; Dibanjo, P.; Vix-Guterl, C.; Martens, T.; Latroche, M. *Faraday Discuss.* **2011**, *115*, 117−131.
(13) Bogdanović, B.; Liao, S.-T.; Schwickardi, M.; Sikorsky, P.; Spliethoff, B. *Angew. Chem., Int. Ed.* **1980**, *19*, 818−819.

(14) Borsa, D. M.; Baldi, A.; Pasturel, M.; Schreuders, H.; Dam, B.; Griessen, R.; Vermeulen, P.; Notten, P. H. L. *Appl. Phys. Lett.* **2006**, *88* (24), 241910−241913.

(15) Vermeulen, P.; Niessen, R. A. H.; Borsa, D. M.; Dam, B.; Griessen, R.; Notten, P. H. L. *Electrochem. Solid-State Lett.* **2006**, *9* (11), A520−A523.

(16) Baldi, A.; Gremaud, R.; Borsa, D. M.; Baldé, C. P.; van der Eerden, A. M. J.; Kruijtzer, G. L.; de Jongh, P. E.; Dam, B.; Griessen, R. *Int. J. Hydrogen Energy* **2009**, *34* (3), 1450−1457.

(17) Baldi, A.; Borsa, D. M.; Schreuders, H.; Rector, J. H.; Atmakidis, T.; Bakker, M.; Zondag, H. A.; van Helden, W. G. J.; Dam, B.; Griessen, R. *Int. J. Hydrogen Energy* **2008**, *33* (12), 3188−3192.

(18) Niessen, R. A. H.; Notten, P. H. L. *Electrochem. Solid-State Lett.* **2005**, *8* (10), A534−A538.

(19) Baldi, A.; Gonzalez-Silveira, M.; Palmisano, V.; Dam, B.; Griessen, R. *Phys. Rev. Lett.* **2009**, *102* (22), 226102.

(20) Asano, K.; Enoki, H.; Akiba, E. *J. Alloys Compd.* **2009**, *480* (2), 558−563.

(21) Asano, K.; Enoki, H.; Akiba, E. *J. Alloys Compd.* **2009**, *478* (1−2), 117−120.

(22) Rousselot, S.; Guay, D.; Roué, L. *J. Power Sources* **2010**, *195* (13), 4370−4374.

(23) Kyoi, D.; Sato, T.; Rönnebro, E.; Kitamura, N.; Ueda, A.; Ito, M.; Katsuyama, S.; Hara, S.; Noréus, D.; Sakai, T. *J. Alloys Compd.* **2004**, *372*, 213−217.

(24) Vons, V.; de Smet, L.; Munao, D.; Evirgen, A.; Kelder, E.; Schmidt-Ott, A. *J. Nanopart. Res.* **2011**, *13* (10), 4867−4879.

(25) Toby, B. H. *J. Appl. Crystallogr.* **2001**, *34* (2), 210−213.

(26) Asano, K.; Enoki, H.; Akiba, E. *J. Alloys Compd.* **2009**, *486* (1−2), 115−123.

(27) Rousselot, S.; Bichat, M. P.; Guay, D.; Roué, L. *J. Electrochem. Soc.* **2009**, *156* (12), A967−A973.

(28) Rönnebro, E.; Kyoi, D.; Kitano, A.; Kitano, Y.; Sakai, T. *J. Alloys Compd.* **2005**, *404−406*, 68−72.

(29) Borsa, D. M.; Gremaud, R.; Baldi, A.; Schreuders, H.; Rector, J. H.; Kooi, B.; Vermeulen, P.; Notten, P. H. L.; Dam, B.; Griessen, R. *Phys. Rev. B* **2007**, *75* (20), 205408.

(30) Rousselot, S.; Bichat, M. P.; Guay, D.; Roué, L. *J. Power Sources* **2008**, *175* (1), 621−624.

(31) Farangis, B.; Nachimuthu, P.; Richardson, T. J.; Slack, J. L.; Perera, R. C. C.; Gullikson, E. M.; Lindle, D. W.; Rubin, M. *Phys. Rev. B* **2003**, *67* (8), 085106.

(32) Yates, K.; West, R. H. *Surf. Interface Anal.* **1983**, *5* (4), 133−138.

(33) Egerton, R. F. Physics of Electron Scattering. In *Electron Energy-Loss Spectroscopy in the Electron Microscope*; Springer: New York: 2011; pp 111−229.

(34) Lisowski, W.; van den Berg, A. H. J.; Leonard, D.; Mathieu, H. J. *Surf. Interface Anal.* **2000**, *29* (4), 292−297.

(35) Farangis, B.; Nachimuthu, P.; Richardson, T. J.; Slack, J. L.; Meyer, B. K.; Perera, R. C. C.; Rubin, M. D. *Solid State Ionics* **2003**, *165* (1−4), 309−314.

(36) Tan, H.; Verbeeck, J.; Abakumov, A.; Van Tendeloo, G. *Ultramicroscopy* **2012**, *116*, 24−33.

(37) Graetz, J.; Ahn, C. C.; Ouyang, H.; Rez, P.; Fultz, B. *Phys. Rev. B* **2004**, *69* (23), 235103.

(38) Mulder, F. M.; Singh, S.; Bolhuis, S.; Eijt, S. W. H. *J. Phys. Chem. C* **2011**, *116* (2), 2001−2012.

(39) Cuevas, F.; Korablov, D.; Latroche, M. *Phys. Chem. Chem. Phys.* **2012**, *14*, 1200−1211.

(40) Gross, K. J.; Spatz, P.; Züttel, A.; Schlapbach, L. *J. Alloys Compd.* **1996**, *240* (1−2), 206−213.

(41) Grzech, A.; Lafont, U.; Magusin, P. C. M. M.; Mulder, F. M. *J. Phys. Chem. C* **2012**, *116*, 26027−26035.

(42) Wang, W.-E. *J. Alloys Compd.* **1996**, *238*, 6−12.

(43) Lu, J.; Choi, Y. J.; Fang, Z. Z.; Sohn, H. Y.; Rönnebro, E. *J. Am. Chem. Soc.* **2010**, *132* (19), 6616−6617.

(44) Lu, J.; Choi, Y. J.; Fang, Z. Z.; Sohn, H. Y.; Rönnebro, E. *J. Am. Chem. Soc.* **2009**, *131* (43), 15843−15852.

(45) Gremaud, R.; Broedersz, C. P.; Borsa, D. M.; Borgschulte, A.; Maron, P.; Schreuders, H.; Rector, J. H.; Dam, B.; Griessen, R. *Adv. Mater.* **2007**, *19*, 2813−2817.

(46) Gremaud, R.; Baldi, A.; Gonzalez-Silveira, M.; Dam, B.; Griessen, R. *Adv. Mater.* **2007**, *19*, 2813−2817.

(47) Krozer, A.; Kasemo, B. *J. Less-Common Met.* **1990**, *160*, 323−342.

(48) Leegwater, H.; Schut, H.; Egger, W.; Baldi, A.; Dam, B.; Eijt, S. W. H. *Appl. Phys. Lett.* **2010**, *96*, 121902.

(49) Wagemans, R. W. P.; van Lenthe, J. H.; de Jongh, P. E.; van Dillen, A. J.; de Jong, K. P. *J. Am. Chem. Soc.* **2005**, *127* (47), 16675−16680.

(50) Er, S.; Tiwari, D.; de Wijs, G. A.; Brocks, G. *Phys. Rev. B* **2009**, *79* (2), 024105.

(51) Er, S.; de Wijs, G. A.; Brocks, G. *J. Phys. Chem. Lett.* **2010**, *1* (13), 1982−1986.

(52) Song, Y.; Guo, Z. X.; Yang, R. *Phys. Rev. B* **2004**, *69* (9), 094205.

(53) Mooij, L. P. A.; Baldi, A.; Boelsma, C.; Shen, K.; Wagemaker, M.; Pivak, Y.; Schreuders, H.; Griessen, R.; Dam, B. *Adv. Energy Mater.* **2011**, *1* (5), 754−758.

(54) Hao, S.; Sholl, D. S. *J. Phys. Chem. C* **2011**, *116* (2), 2045−2050.

(55) Zhao-Karger, Z.; Hu, J.; Roth, A.; Wang, D.; Kübel, C.; Lohstroh, W.; Fichtner, M. *Chem. Commun.* **2010**, *46*, 8353−8355.

(56) Berube, V.; Chen, G.; Dresselhaus, M. S. *Int. J. Hydrogen Energy* **2008**, *33* (15), 4122−4131.

(57) Berube, V.; Dresselhaus, M. S.; Chen, G. *Int. J. Hydrogen Energy* **2009**, *34* (4), 1862−1872.

(58) Berube, V.; Dresselhaus, M. S.; Chen, G. *Int. J. Hydrogen Energy* **2008**, *33* (20), 5617−5628.

(59) Varin, R. A.; Czujko, T.; Chiu, C.; Wronski, Z. *J. Alloys Compd.* **2006**, *424* (1−2), 356−364.

(60) Varin, R. A.; Jang, M.; Czujko, T.; Wronski, Z. S. *J. Alloys Compd.* **2010**, *493* (1−2), L29−L32.